HYBRID ESSENTIALLY NON-OSCILLATORY SCHEMES FOR HYPERBOLIC CONSERVATION LAWS

RAIMUND BÜRGER[A] AND DAVID ZORÍO[B,*]

Abstract. A novel family of high-order shock-capturing schemes is defined by combining high-order and low-order (first-order) reconstructions of numerical fluxes through a single non-linear, scale-independent and non-dimensional weight. This weight is designed to attain the desired order of accuracy near smooth data and to reduce the scheme to first order near discontinuities, and involves a tuning parameter that introduces a degree of tolerance towards high gradients. The resulting hybrid essentially non-oscillatory (HENO) reconstruction is easy to implement on unstructured meshes and is computationally cheap, especially on uniform meshes, in which the number of operations grows linearly with respect to the order. Numerical experiments for solving hyperbolic conservation laws with discontinuous solutions in one and two space dimensions illustrate that if the tuning parameter of HENO reconstructions is chosen properly, then a scheme of this type attains similar or even better results than weighted essentially non-oscillatory (WENO) schemes of the same formal order of accuracy, but does so at a lower computational cost.

1. Introduction

1.1. **Scope.** High-order shock-capturing schemes are widely used to approximate discontinuous solutions of hyperbolic conservation laws. One of the most successful techniques to achieve such goal are the well-known weighted essentially non-oscillatory (WENO) reconstruction techniques [9] to obtain high-order approximations of numerical fluxes, for instance in the context of finite difference [11, 12] and finite volume schemes [5].

These techniques are based on the construction of nonlinear weights in such a way that the oscillatory behaviour near discontinuities is avoided. These oscillations are caused by the usage of high-order polynomials near data with abrupt changes. Such weights have been redesigned in the literature, most notably by Jiang and Shu [8] who redesigned the non-linear weights in such a way that the optimal order of accuracy was achieved on smooth zones. Later improvements of the order of accuracy near critical points and of the resolution near discontinuities include [3, 6, 15, 16].

It is the purpose of the present work to introduce a simplification of traditional WENO methods. While these methods employ multiple weights conveniently designed to obtain an optimal-order convex combination of interpolation polynomials near smooth zones and an essentially non-oscillatory behaviour near discontinuities, we herein define one single weight that directly acts as a "switch" between the optimal-order reconstruction polynomial and a low-order (first-order) reconstruction. The resulting method will be addressed as "Hybrid Essentially Non-Oscillatory (HENO) method." This contribution is partly motivated by a comment by Borges et al. [3], where the authors introduce WENO-Z schemes and in their conclusion state [3, p. 3210]: "Our analysis also indicated

Date: October 12, 2018.

Key words and phrases. shock-capturing schemes, hybrid essentially non-oscillatory methods, conservation laws.

*Corresponding author.

[A] CI^{2}MA and Departamento de Ingeniería Matemática, Universidad de Concepción, Casilla 160-C, Concepción, Chile. E-Mail: rburger@ing-mat.udec.cl.

[B] CI^{2}MA, Universidad de Concepción, Casilla 160-C, Concepción, Chile. E-Mail: dzorio@ci2ma.udec.cl.

that the improvements obtained by the mapped WENO over the classical scheme when solving problems with shocks are not due to its superior accuracy at critical points of the solutions, but to the larger weights it assigns to stencils with discontinuities. Similarly, the new WENO scheme assigns even larger weights to discontinuous stencils, obtaining solutions that are sometimes sharper, although its rate of convergence at critical points is intermediary between those schemes." We herein take to an extreme this consideration and design a weight with a tuning parameter allowing reconstructions with optimal order *almost everywhere*, in the sense that this weight will favour the low-order reconstruction near sharp discontinuities only; moreover, we will show that in that case it is sufficient to limit the scheme to first order to achieve desirable results, as long as the high-order reconstructions are predominant near smooth zones or smeared discontinuities.

1.2. **Outline of this paper.** The remainder of the paper is organized as follows. In Section 2 the HENO approach is presented. Although we focus on numerical experiments with finite-difference methods for hyperbolic conservation laws on Cartesian grids, we introduce in Section 2.1 arbitrary (non-uniform) grids, and present in Section 2.2 the general HENO approach for arbitrary grids and any type of reconstruction (both from cell averages and from point values), since this generality does not lead to any additional difficulty. Section 2.2 also contains the main theoretical result, Theorem 2.1 and its proof, which states the accuracy properties of the HENO reconstruction that for data taken from a sufficiently smooth function. The corresponding algorithm is summarized in Section 2.3. In Section 2.4 we outline the HENO reconstruction for a uniform grid, for which some of the terms appearing in the general non-uniform case can be simplified. Section 3 is devoted to a series of numerical experiments in which HENO schemes are compared in terms of accuracy and efficiency with some common WENO methods in the context of hyperbolic conservation laws. In Example 1 (Section 3.1) the HENO reconstruction is applied to a linear advection equation with known exact smooth solution to verify that the observed order of accuracy is consistent with the theoretical analysis. Section 3.2 presents results for the Shu-Osher problem of the one-dimensional (1D) Euler equations of gas dynamics (Example 2), including a study of the effect of the variation of the HENO design parameter and a comparison between third- and fifth-order HENO and WENO schemes. In Section 3.3 we consider the Sod shock tube problem for the 1D Euler equations of gas dynamics (Example 3), with a focus on comparison between third- and fifth-order HENO and WENO schemes. Section 3.4 presents similar results for the Lax shock tube problem for the 1D Euler equations of gas dynamics (Example 4). Sections 3.5 and 3.6 (Examples 5 and 6) are devoted to the 2D Euler equations of gas dynamics. Results are presented for the scenarios of Double Mach reflection and of a Riemann problem. Finally, conclusions are collected in Section 4.

2. Hybrid Essentially Non-Oscillatory (HENO) reconstructions

2.1. **Preliminaries.** Consider a stencil of R cells, obtained by the interfaces

$$x_{i-1/2,h} = z + c_{i-1/2}h, \quad z, c_{i-1/2} \in \mathbb{R}, \quad c_{i-1/2} < c_{j-1/2} \text{ if } i < j,\ 0 \le i \le R. \tag{2.1}$$

within a not necessarily equidistant grid on $\mathbb{R}$.

Let $c_i := \frac{1}{2}(c_{i-1/2} + c_{i+1/2})$, and denote by $x_{i,h} := z + c_i h$, $0 \le i \le R-1$, the corresponding cell centers. Let $f : D \to \mathbb{R}$ be function with $[x_{-1/2,h}, x_{R-1/2,h}] \subseteq D$, and we wish to apply the reconstruction either to point values

$$f_{i,h} := f(x_{i,h}), \quad 0 \le i \le R-1, \tag{2.2}$$

or to cell averages

$$f_{i,h} := \frac{1}{x_{i+1/2,h} - x_{i-1/2,h}} \int_{x_{i-1/2,h}}^{x_{i+1/2,h}} f(x)\,\mathrm{d}x, \quad 0 \le i \le R-1. \tag{2.3}$$

We denote by p_R the unique interpolating polynomial of degree at most $R-1$ that satisfies either

$$p_R(x_{i,h}) = f_{i,h}, \quad 0 \le i \le R-1 \tag{2.4}$$

for reconstructions from point values (2.2) or

$$\frac{1}{x_{i+1/2,h} - x_{i-1/2,h}} \int_{x_{i-1/2,h}}^{x_{i+1/2,h}} p_R(x)\,\mathrm{d}x = f_{i,h}, \quad 0 \le i \le R-1 \tag{2.5}$$

for reconstructions from cell averages (2.3). If we wish to approximate f at a given point $x^* \in D$, then if $f \in C^R$, then there holds $p_R(x^*) = f(x^*) + \mathcal{O}(h^R)$ as $h \to 0$.

2.2. **General HENO approach.** We define a non-linear and data-dependent weight to hybridize the reconstruction, keeping the high order near smooth zones and turning to first order near discontinuities. To this end, we define terms that measure smoothness. Let

$$r = \lfloor (R-1)/2 \rfloor, \quad s = R - 1 - 2r. \tag{2.6}$$

We then define the two one-sided smoothness indicators

$$I_R^{\mathrm{L}} := \sum_{i=0}^{r-1} \left(\frac{f_{i+1,h} - f_{i,h}}{c_{i+1} - c_i} \right)^2 \quad \text{and} \quad I_R^{\mathrm{R}} := \sum_{i=r+s}^{R-2} \left(\frac{f_{i+1,h} - f_{i,h}}{c_{i+1} - c_i} \right)^2 \tag{2.7}$$

that correspond to the left and the right part of the stencil, respectively. Now, the square of the undivided difference of maximum order is defined by

$$\tau_R := \big(f[x_{0,h}, \ldots, x_{R-1,h}] \big)^2, \tag{2.8}$$

which is obtained inductively through the recurrence

$$\begin{aligned} f[x_{i,h}] &= f_{i,h}, \\ f[x_{i,h}, \ldots, x_{j,h}] &= \frac{f[x_{i+1,h}, \ldots, x_{j,h}] - f[x_{i,h}, \ldots, x_{j-1,h}]}{c_j - c_i}. \end{aligned} \tag{2.9}$$

The weight with hybridization parameter $\lambda \in [0,1]$ is then given by

$$\omega_\lambda := \frac{\lambda (I_R^{\mathrm{L}} I_R^{\mathrm{R}} + \varepsilon)}{\lambda I_R^{\mathrm{L}} I_R^{\mathrm{R}} + (1-\lambda)(I_R^{\mathrm{L}} + I_R^{\mathrm{R}})\tau_R + \varepsilon}, \tag{2.10}$$

where $\varepsilon > 0$ is a small quantity to prevent divisions by zero if the data is constant or nearly constant. (In our numerical experiments we will take $\varepsilon = 10^{-100}$.)

The low-order reconstruction consists in taking the closest value of the data from the stencil with respect to the extrapolation point. Namely, we choose $f_{i_0,h}$, where

$$i_0 := \operatorname*{argmin}_{0 \le i \le R-1} |x_{i,h} - x^*|. \tag{2.11}$$

The HENO reconstruction is then defined by

$$q_R(x^*) := \omega_\lambda p_R(x^*) + (1 - \omega_\lambda) f_{i_0,h}. \tag{2.12}$$

Remark 2.1. *The parameter λ is a term which polarizes the weight ω_λ towards zero as $\lambda \to 0^+$ (and thus, polarizing $q_R(x^*)$ towards $f_{i_0,h}$) and polarizes the weight ω_λ towards one as $\lambda \to 1^-$ (therefore, polarizing $q_R(x^*)$ towards $p_R(x^*)$). The limiting case $\lambda = 0$ leads to $\omega_\lambda = 0$ regardless of the data, and thus $q_R(x^*) = f_{i_0,h}$. On the other hand, if $\lambda = 1$, then $\omega_\lambda = 1$ regardless of the data, and hence $q_R(x^*) = p_R(x^*)$.*

Definition 2.1. *Let $\kappa \in \mathbb{N}$, $f \in C^{\kappa+1}$ and $z \in \mathbb{R}$. We say that z is a critical point of order κ of f if $f^{(s)}(z) = 0$ for $1 \leq s \leq \kappa$ and $f^{(\kappa+1)}(z) \neq 0$.*

The accuracy properties are next analyzed.

Theorem 2.1. *For any $\lambda \in [0, 1]$, there holds $0 \leq \omega_\lambda \leq 1$.*

Furthermore, if $f \in C^R$ with a critical point of order κ at z, then for $0 < \lambda \leq 1$ there holds

$$q_R(x^*) = \begin{cases} f(x^*) + \mathcal{O}(h^R) & \text{if } \kappa < R - 2 - \beta, \\ f(x^*) + \mathcal{O}(h^{\kappa+1}) & \text{if } \kappa \geq R - 2 - \beta, \end{cases}$$

where $\beta = 1$ if $R = 4$ and $\beta = 0$ otherwise. On the other hand, if a discontinuity crosses the data of the stencil from which f is sampled and $0 \leq \lambda < 1$, then $q_R(x^*) = f(x^*) + \mathcal{O}(h)$.

Proof. Clearly, there holds

$$0 \leq \omega_\lambda = \frac{\lambda(I_R^{\mathrm{L}} I_R^{\mathrm{R}} + \varepsilon)}{\lambda I_R^{\mathrm{L}} I_R^{\mathrm{R}} + (1-\lambda)(I_R^{\mathrm{L}} + I_R^{\mathrm{R}})\tau_R + \varepsilon} \leq \frac{\lambda I_R^{\mathrm{L}} I_R^{\mathrm{R}} + \lambda\varepsilon}{\lambda I_R^{\mathrm{L}} I_R^{\mathrm{R}} + \varepsilon} \leq 1.$$

For simplicity, we now drop the role of ε.

Let us first assume that the stencil is smooth. Then for $3 \leq R \leq 4$, the one-sided smoothness indicators (2.7) are given by $I_R^{\mathrm{L}} = (f_{1,h} - f_{0,h})^2$ and $I_R^{\mathrm{R}} = (f_{R-1,h} - f_{R-2,h})^2$. For $\kappa = 0$, there hold $I_R^{\mathrm{L}} = \mathcal{O}(h^2)$ and $I_R^{\mathrm{R}} = \mathcal{O}(h^2)$ as $h \to 0$. Consequently,

$$\omega_\lambda = \frac{\lambda I_R^{\mathrm{L}} I_R^{\mathrm{R}}}{\lambda I_R^{\mathrm{L}} I_R^{\mathrm{R}} + (1-\lambda)(I_R^{\mathrm{L}} + I_R^{\mathrm{R}})\tau_R} = \frac{1}{1 + \dfrac{1-\lambda}{\lambda} \dfrac{I_R^{\mathrm{L}} + I_R^{\mathrm{R}}}{I_R^{\mathrm{L}} I_R^{\mathrm{R}}} \tau_R} \tag{2.13}$$

implies that

$$\omega_\lambda = \frac{1}{1 + \dfrac{1-\lambda}{\lambda} \dfrac{\mathcal{O}(h^2) + \mathcal{O}(h^2)}{\mathcal{O}(h^2)\mathcal{O}(h^2)} \mathcal{O}(h^{2R-2})} = \frac{1}{1 + \dfrac{1-\lambda}{\lambda} \mathcal{O}(h^{2R-4})} = 1 - \mathcal{O}(h^{2R-4}),$$

and therefore

$$\begin{aligned} q_R(x^*) &= \omega_\lambda p_R(x^*) + (1-\omega_\lambda) f_{i_0,h} = \omega_\lambda \big(f(x^*) + \mathcal{O}(h^R)\big) + (1-\omega_\lambda)\big(f(x^*) + \mathcal{O}(h)\big) \\ &= f(x^*) + \omega_\lambda \mathcal{O}(h^R) + (1-\omega_\lambda)\mathcal{O}(h) = f(x^*) + \big(1 - \mathcal{O}(h^{2R-4})\big)\mathcal{O}(h^R) + \mathcal{O}(h^{2R-4})\mathcal{O}(h) \\ &= f(x^*) + \mathcal{O}(h^R) + \mathcal{O}(h^{2R-3}) = f(x^*) + \mathcal{O}(h^R), \end{aligned}$$

where the last equality holds since $2R - 3 \geq R$ for $R \geq 3$.

Let us now assume $R > 4$ with $\kappa < R - 2$. Then, by the arguments of [2, Lemma 3], there hold $I_R^{\mathrm{L}} = \mathcal{O}(h^{2\kappa+2})$ and $I_R^{\mathrm{R}} = \mathcal{O}(h^{2\kappa+2})$, hence from (2.13) we now get

$$\omega_\lambda = \frac{1}{1 + \dfrac{1-\lambda}{\lambda} \dfrac{\mathcal{O}(h^{2\kappa+2}) + \mathcal{O}(h^{2\kappa+2})}{\mathcal{O}(h^{2\kappa+2})\mathcal{O}(h^{2\kappa+2})} \mathcal{O}(h^{2R-2})} = \frac{1}{1 + \dfrac{1-\lambda}{\lambda} \mathcal{O}(h^{2R-2\kappa-4})} = 1 - \mathcal{O}(h^{2R-2\kappa-4}).$$

Therefore,

$$\begin{aligned} q_R(x^*) &= \omega_\lambda p_R(x^*) + (1-\omega_\lambda) f_{i_0,h} = \omega_\lambda\big(f(x^*) + \mathcal{O}(h^R)\big) + (1-\omega_\lambda)\big(f(x^*) + \mathcal{O}(h^{\kappa+1})\big) \\ &= f(x^*) + \omega_\lambda \mathcal{O}(h^R) + (1-\omega_\lambda)\mathcal{O}(h^{\kappa+1}) \\ &= f(x^*) + \big(1 - \mathcal{O}(h^{2R-2\kappa-4})\big)\mathcal{O}(h^R) + \mathcal{O}(h^{2R-2\kappa-4})\mathcal{O}(h^{\kappa+1}) \\ &= f(x^*) + \mathcal{O}(h^R) + \mathcal{O}(h^{2R-\kappa-3}) = f(x^*) + \mathcal{O}(h^R), \end{aligned}$$

where the last equality holds since by assumption $\kappa < R-2$, and thus $2R-\kappa-3 \geq R$.

The final case for the assumption of smoothness concerns the case $\kappa \geq R-2$ and $\kappa \geq R-3$ for $R=4$. In this case, the weight ω_λ does not necessarily converge to 1, and thus the only result that can be concluded is

$$\begin{aligned} q_R(x^*) &= \omega_\lambda p_R(x^*) + (1-\omega_\lambda) f_{i_0,h} \\ &= \omega_\lambda\big(f(x^*) + \mathcal{O}(h^{\max\{R,\kappa+1\}})\big) + (1-\omega_\lambda)\big(f(x^*) + \mathcal{O}(h^{\kappa+1})\big) \\ &= f(x^*) + \omega_\lambda \mathcal{O}(h^{\max\{R,\kappa+1\}}) + (1-\omega_\lambda)\mathcal{O}(h^{\kappa+1}) = f(x^*) + \mathcal{O}(h^{\kappa+1}). \end{aligned}$$

Finally, let us assume that a discontinuity crosses the data. Then, since the one-sided smoothness indicators are computed on non-overlapping zones, one has either $I_R^{\mathrm{L}} = \mathcal{O}(1)$ and $I_R^{\mathrm{R}} = \mathcal{O}(h^2)$ (if the discontinuity crosses the first half of the stencil) or $I_R^{\mathrm{L}} = \mathcal{O}(h^2)$ and $I_R^{\mathrm{R}} = \mathcal{O}(1)$ (if the discontinuity crosses the second half side of the stencil). In both cases, there hold $I_R^{\mathrm{L}} + I_R^{\mathrm{R}} = \mathcal{O}(1)$, $\tau_R = \mathcal{O}(1)$ and $I_R^{\mathrm{L}} I_R^{\mathrm{R}} = \mathcal{O}(h^2)$. Therefore (2.13) now implies that

$$\omega_\lambda = \frac{1}{1 + \dfrac{1-\lambda}{\lambda}\dfrac{\mathcal{O}(1)\mathcal{O}(1)}{\mathcal{O}(h^2)}} = \frac{1}{1 + \dfrac{1-\lambda}{\lambda}\mathcal{O}(h^{-2})} = 1 - \mathcal{O}(h^2),$$

hence

$$q_R(x^*) = \omega_\lambda p_R(x^*) + (1-\omega_\lambda) f_{i_0,h} = \mathcal{O}(h^2)\mathcal{O}(1) + \big(1 - \mathcal{O}(h^2)\big)\big(f(x^*) + \mathcal{O}(h)\big) = f(x^*) + \mathcal{O}(h).$$

This concludes the proof. □

Remark 2.2. *Theorem 2.1 implies that the cases in which the accuracy of the hybrid scheme drops below the optimal accuracy order, R, are $\kappa = R-2$ for $R \neq 4$, in which the accuracy drops to order $R-1$, and $1 \leq \kappa \leq 2$ for $R=4$, where the accuracy drops to order 2 and 3, respectively.*

2.3. **Summary of the algorithm.** The steps of the HENO reconstruction algorithm are summarized below.

Input: nodes $x_{i-1/2,h}$ given by (2.1), nodal values $f_{i,h}$ given either as point values (2.2) or cell averages (2.3), reconstruction point x^*, hybridization parameter $\lambda \in [0,1]$, and $\varepsilon > 0$.

(1) Compute the reconstruction polynomial p_R associated to the whole data from the stencil, and evaluate it at x^*. The polynomial p_R is supposed to satisfy either (2.4) for reconstructions from point values or (2.5) for reconstructions from cell averages.
(2) Find the nodal value $f_{i_0,h}$ corresponding to the node closest to x^*, where the index i_0 satisfies (2.11).
(3) Compute the left and right smoothness indicators I_R^{L} and I_R^{R} given by (2.6) and (2.7).
(4) Compute the square of the undivided difference of maximum order τ_R defined by (2.8) and (2.9).
(5) Obtain the weight ω_λ with hybridization parameter λ from (2.10).
(6) Compute the hybrid reconstruction $q_R(x^*)$ from (2.12).

Output: HENO reconstruction: $q_R(x^*)$.

2.4. **HENO reconstruction on uniform meshes with $2r-1$ nodes.** We assume that the grid is now composed of $2r-1$ nodes of the form $x_{i,h} = z + (c+i)h$, $-r+1 \leq i \leq r-1$, with $c \in \mathbb{R}$. These nodes represent cell centers. If we assume, for instance, right-biased reconstructions at the cell interface $x_{1/2}$, then $i_0 = 0$, i.e., we can choose as the closest node the central one, that is $x_{0,h}$, with the corresponding nodal value $f_{0,h}$. Then $p_{2r-1}(x_{1/2})$ can be computed as a linear combination of $f_{i,h}$ with constant coefficients in both cases of reconstruction from point values and cell averages, as we describe next in the algorithm steps.

Input: nodal values $f_{i,h}$, $-r+1 \leq i \leq r-1$, hybridization parameter $\lambda \in [0,1]$, and $\varepsilon > 0$.

(1) Compute $p_{2r-1}(x_{1/2})$, which can be written as

$$p_{2r-1}(x_{1/2}) = \sum_{i=-r+1}^{r-1} \alpha_i f_{i,h}, \quad \text{where} \quad \alpha_i := \frac{(-1)^{i-1} r}{2^{4r-3}(2i-1)} \binom{2r}{r} \binom{2r-2}{i+r-1} f_{i,h},$$

in the case of reconstructions from point values and

$$\alpha_i := \begin{cases} -\binom{2r-1}{r-1}^{-1} \displaystyle\sum_{j=-i+1}^{r} \frac{(-1)^j}{j} \binom{2r-1}{r-1+j} & \text{for } i \leq 0, \\ -\binom{2r-1}{r-1}^{-1} \displaystyle\sum_{j=i}^{r-1} \frac{(-1)^j}{j} \binom{2r-1}{r-1-j} & \text{for } i > 0 \end{cases}$$

in the case of reconstructions from cell averages [1, Proposition 1].

(2) Compute the left and right smoothness indicators

$$I^{\mathrm{L}}_{2r-1} = \sum_{i=-r+1}^{0} (f_{i+1,h} - f_{i,h})^2, \quad I^{\mathrm{R}}_{2r-1} = \sum_{i=0}^{r-1} (f_{i+1,h} - f_{i,h})^2.$$

(3) Compute the square of the undivided difference of maximum order. We here obtain

$$\tau_{2r-1} = \left(\sum_{i=-r+1}^{r-1} (-1)^{i-r+1} \binom{2r-2}{i+r-1} f_{i,h} \right)^2.$$

(4) Obtain the weight ω_λ with hybridization parameter λ. Here we get

$$\omega_\lambda = \frac{\lambda(I^{\mathrm{L}}_{2r-1} I^{\mathrm{R}}_{2r-1} + \varepsilon)}{\lambda I^{\mathrm{L}}_{2r-1} I^{\mathrm{R}}_{2r-1} + (1-\lambda)(I^{\mathrm{L}}_{2r-1} + I^{\mathrm{R}}_{2r-1})\tau_{2r-1} + \varepsilon}.$$

(5) Compute the hybrid reconstruction $q_{2r-1}(x_{1/2}) = \omega_\lambda p_{2r-1}(x_{1/2}) + (1-\omega_\lambda) f_{0,h}$.

Output: HENO reconstruction: $q_{2r-1}(x_{1/2})$.

3. Numerical experiments

The hybrid scheme combines a low order scheme, based on first-order reconstructions (case $\lambda = 0$), with a linear high-order scheme, based on reconstructions of order $2r-1$ (case $\lambda = 1$). As it has been shown when $0 < \lambda < 1$, the resulting scheme is formally speaking a high-order one (because $\lambda > 0$), while having non-oscillatory properties near discontinuities (because $\lambda < 1$). However, it is expected that the closer to zero λ is chosen, the less sharp the numerical solution will become, while the closer to one λ is chosen, the sharper its resolution will become. Nonetheless, one must be careful in the latter case, since the closer the parameter λ is to 1, the greater is the risk of appearance of osillations near discontinuities. Despite that consideration, we will see that the

	JS-WENO5				YC-WENO5				HENO5, $\lambda = 0$			
	$\|\cdot\|_1$		$\|\cdot\|_\infty$		$\|\cdot\|_1$		$\|\cdot\|_\infty$		$\|\cdot\|_1$		$\|\cdot\|_\infty$	
N	Err.	$\mathcal{O}$	Err.	$\mathcal{O}$	Err.	$\mathcal{O}$	Err.	$\mathcal{O}$	Err.	$\mathcal{O}$	Err.	$\mathcal{O}$
20	3.56e-04	—	6.85e-04	—	3.27e-05	—	5.16e-05	—	1.25e-01	—	1.94e-01	—
40	1.09e-05	5.03	2.37e-06	4.86	1.01e-06	5.01	1.60e-06	5.01	6.98e-02	0.84	1.09e-01	0.83
80	3.31e-07	5.04	7.02e-08	5.08	3.15e-08	5.01	4.94e-08	5.01	3.70e-02	0.92	5.80e-02	0.91
160	1.03e-08	5.00	2.21e-09	4.99	9.79e-10	5.01	1.54e-09	5.01	1.90e-02	0.96	2.99e-02	0.96
320	3.22e-10	5.00	6.65e-11	5.06	3.05e-11	5.00	4.79e-11	5.00	9.67e-03	0.98	1.52e-02	0.98
640	1.01e-11	5.00	2.02e-12	5.04	9.53e-13	5.00	1.50e-12	5.00	4.87e-03	0.99	7.65e-03	0.99
	HENO5, $\lambda = 0.5$				HENO5, $\lambda = 0.9$				HENO5, $\lambda = 1$			
	$\|\cdot\|_1$		$\|\cdot\|_\infty$		$\|\cdot\|_1$		$\|\cdot\|_\infty$		$\|\cdot\|_1$		$\|\cdot\|_\infty$	
N	Err.	$\mathcal{O}$	Err.	$\mathcal{O}$	Err.	$\mathcal{O}$	Err.	$\mathcal{O}$	Err.	$\mathcal{O}$	Err.	$\mathcal{O}$
20	1.12e-03	—	2.41e-03	—	1.27e-04	—	3.90e-04	—	3.27e-05	—	5.16e-05	—
40	2.06e-05	5.76	9.42e-05	4.68	2.17e-06	5.88	1.15e-05	5.09	1.01e-06	5.01	1.60e-06	5.02
80	2.95e-07	6.13	2.55e-06	5.21	4.57e-08	5.57	3.14e-07	5.19	3.15e-08	5.01	4.94e-08	5.01
160	4.49e-09	6.04	6.45e-08	5.30	1.13e-09	5.33	8.46e-09	5.21	9.79e-10	5.01	1.54e-09	5.01
320	7.77e-11	5.85	1.70e-09	5.25	3.20e-11	5.15	2.31e-10	5.20	3.05e-11	5.00	4.79e-11	5.00
640	1.56e-12	5.64	4.41e-11	5.27	9.66e-13	5.05	6.22e-12	5.21	9.53e-13	5.00	1.50e-12	5.00

TABLE 1. Example 1 (linear advection equation): fifth-order schemes.

optimal parameters of λ seem to be values very close to 1, in which the essentially non-oscillatory properties are still attained while acting like a genuine scheme of order $2r-1$.

In fact, we will see that these optimal values of λ are valid for any experiment for a scheme of fixed order, and therefore once it is properly tuned, there is no need to tune it again for different problems. Moreover, we will also see that that a HENO scheme of order r attains similar results than a WENO scheme of order $2r-1$, having thus a heavy impact in terms of computational efficiency. In these cases, the error will be computed in density using the L_1-norm, $\|\cdot\|_1$, through reference solutions computed on a fine mesh.

In all the numerical experiments we denote $N = \ell/h$, where ℓ is length of the domain interval.

3.1. **Example 1: linear advection equation.** We consider first the linear advection equation $u_t + u_x = 0$ with a smooth initial condition $u_0(x) = 0.25 + 0.5\sin(\pi x)$ such that the periodic exact solution is given by $u(x,t) = 0.25 + 0.5\sin(\pi(x-t))$. We simulate up to final time $T = 1$ and compare the results obtained by the fifth-order JS-WENO and YC-WENO schemes with those obtained by the HENO reconstruction with several values of the hybridization parameter, namely $\lambda \in \{0, 0.5, 0.9, 1\}$, where we recall that $\lambda = 0$ and $\lambda = 1$ correspond to the first-order scheme and the formal fifth-order scheme, respectively. In this example, the fifth-order approximate Lax-Wendroff scheme [17] is used for the time discretization. For Example 1, the results, shown in Table 1, are consistent with the theoretical result (see Section 2.2) stating that for $0 < \lambda \leq 1$ the resulting scheme has order $2r-1$, while the accuracy drops to first order when $\lambda = 0$.

3.2. **Example 2: 1D Euler equations of gas dynamics, Shu-Osher problem.** The 1D Euler equations of gas dynamics are given by $\boldsymbol{u}_t + \boldsymbol{f}(\boldsymbol{u})_x = \boldsymbol{0}$ for $\boldsymbol{u} = (\rho, \rho v, E)^{\mathrm{T}}$ and $\boldsymbol{f}(\boldsymbol{u}) = (\rho v, p + \rho v^2, v(E+p))^{\mathrm{T}}$, where ρ is the density, v is the velocity, E is the specific energy and p is the pressure of the gas. The partial differential equations are complemented by the equation of state

$$p = (\gamma - 1)\left(E - \frac{1}{2}\rho v^2\right),$$

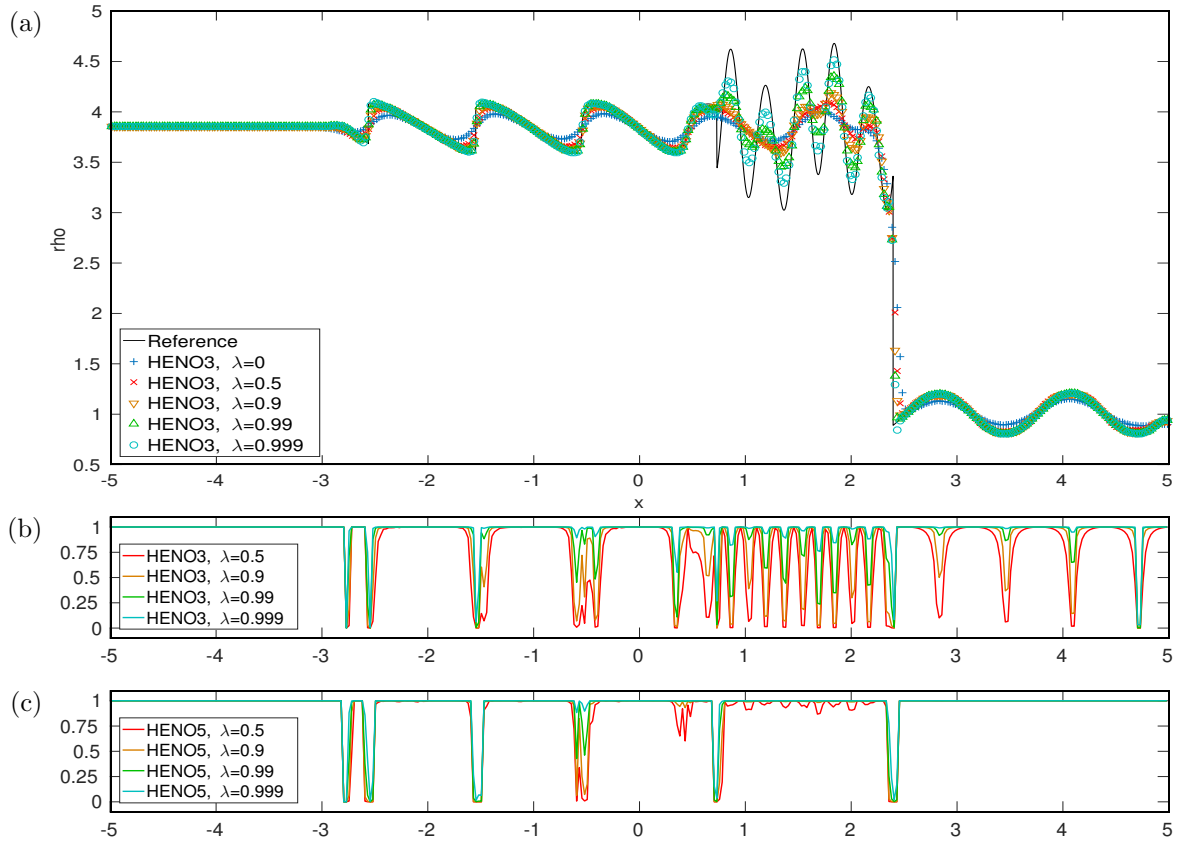

FIGURE 1. Example 2a (Shu-Osher problem, 1D Euler equations of gas dynamics): (a) numerical solution with $N = 400$ at $T = 1.8$ produced by third-order HENO schemes with several values of λ, (b) corresponding weights ω_λ, (c) weights ω_λ corresponding to fifth-order HENO schemes for the same scenarios (numerical solution not shown here).

where γ is the adiabatic constant that will be taken as $\gamma = 1.4$. The spatial domain is $\Omega := (-5, 5)$, and the initial condition is

$$(\rho, v, p)(x, 0) = \begin{cases} \left(\dfrac{27}{7}, \dfrac{4\sqrt{35}}{9}, \dfrac{31}{3}\right) & \text{if } x \leq -4, \\ \left(1 + \dfrac{1}{5}\sin(5x), 0, 1\right) & \text{if } x > -4, \end{cases}$$

stipulates the interaction of a Mach 3 shock with a sine wave and is complemented with left inflow and right outflow boundary conditions. We run the simulation until $T = 1.8$ and compare the schemes with a reference solution computed with a resolution of $N = 16000$. In this example and the remaining ones we will use a third order Runge-Kutta TVD for the time discretization, with a Donat-Marquina flux splitting formula for spatial reconstructions [4].

Example 2a: third-order HENO schemes with several values of λ. We start with a test involving third-order HENO-schemes with several values of λ, and with a resolution of $N = 400$ points. The numerical solutions and an efficiency plot provided in Figures 1 and 2 and 3 (a), respectively. These

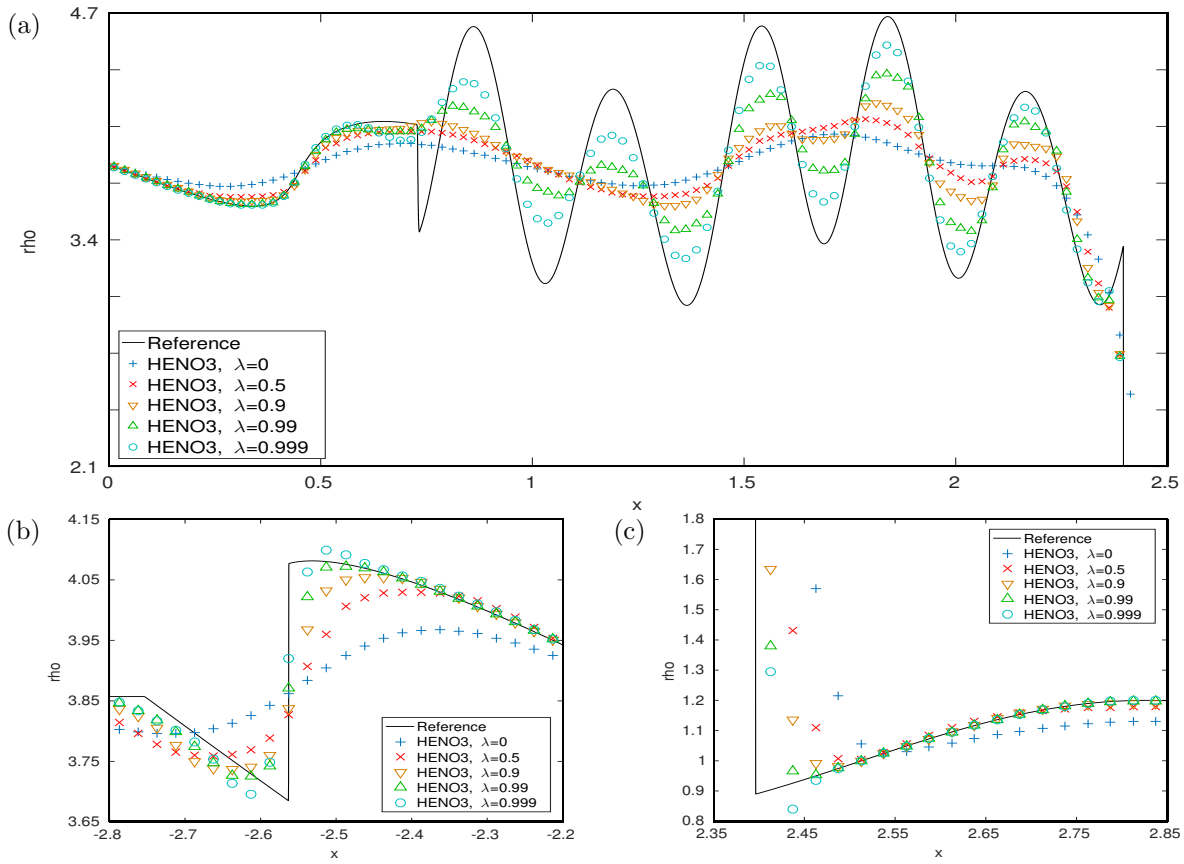

FIGURE 2. Example 2a (Shu-Osher problem, 1D Euler equations of gas dynamics): enlarged views of parts of the numerical solution of Figure 1 (a).

results indicate that HENO schemes allow values of λ very close to one. In fact, the overshoot near the shock seems to appear in the transition between $\lambda = 0.99$ and $\lambda = 0.999$ (since it does not appear for $\lambda = 0.99$ but can be clearly appreciated for $\lambda = 0.999$). On the other hand, there is a clear relationship between the efficiency of the schemes and the (prudential) closeness of the parameter λ to one. In addition, we depict the values of the weights ω_λ for different λ values both for HENO3 and HENO5 schemes in Figures 1 (b) and (c), respectively. The results show that the weights are close to one on smooth zones, drops to values close to zero near singularities (yielding the non-oscillatory behaviour), as well as a remarkable accuracy loss near critical points ($\kappa = 1$) in the case of HENO3 schemes, while being kept by HENO5 in the same regions, which is consistent with the results drawn in Theorem 2.1.

Example 2b: Comparison between third- and fifth-order HENO and WENO schemes. We now fix $\lambda = 0.995$ for both third- and fifth-order HENO schemes and compare the results produced by both schemes with those generated by the corresponding four WENO schemes resulting from the combination of third and fifth order with the Jiang-Shu and Yamaleev-Carpenter weight design. The numerical results are depicted in Figure 4, and the efficiency (numerical error versus CPU time) is plotted in Figure 3 (b). The results show that with our parameter choice, the third-order HENO schemes have better resolution and, in fact, efficiency, than their corresponding WENO

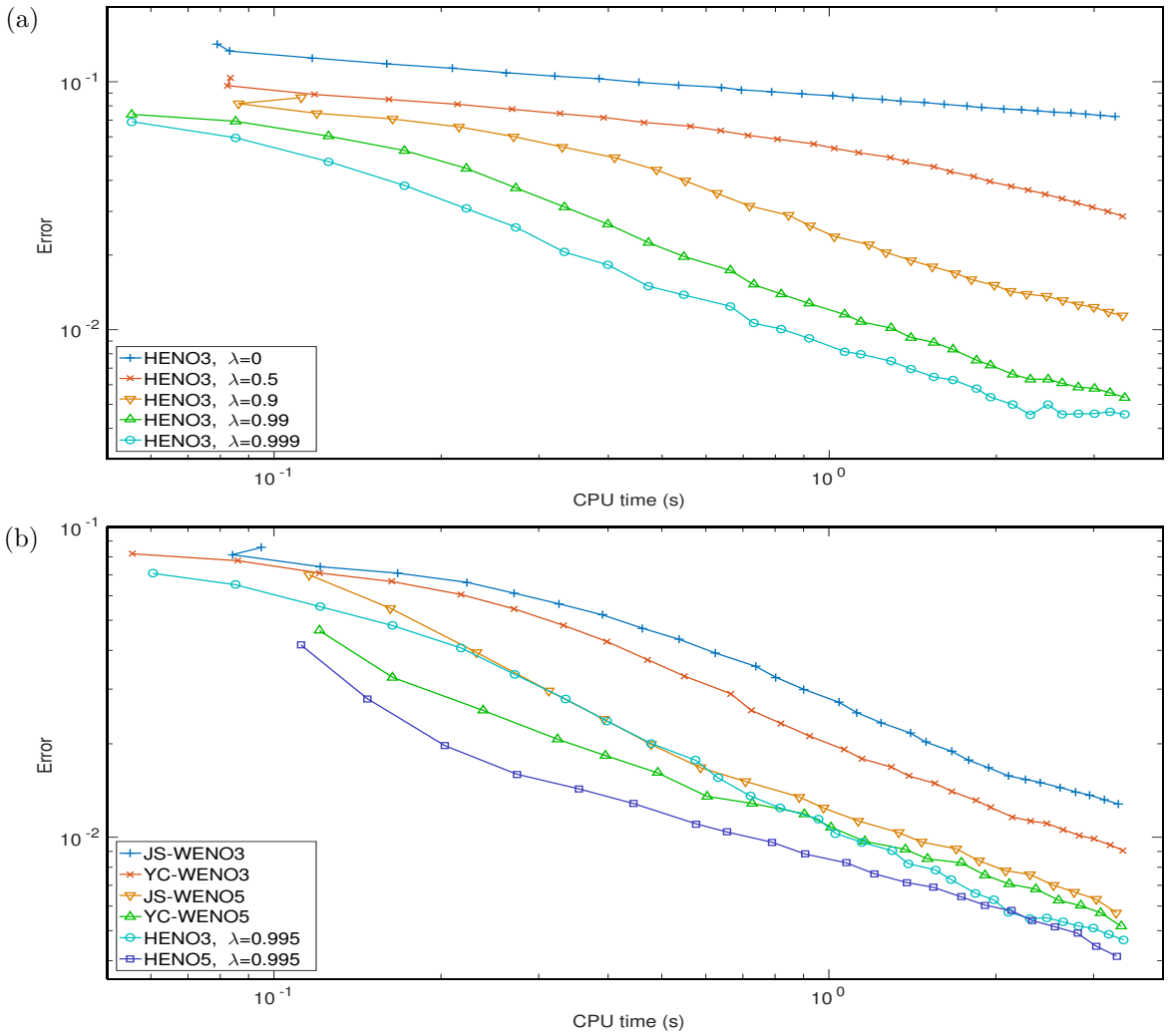

FIGURE 3. Examples 2a and 2b (Shu-Osher problem, 1D Euler equations of gas dynamics): efficiency (for approximation of the solution at $T = 1.8$) of the schemes (a) of Example 2a, (b) of Example 2b.

counterparts. Moreover, they are more efficient than fifth-order JS-WENO scheme and even fifth-order YC-WENO scheme on fine resolutions. Furthermore, we can observe that the fifth-order HENO scheme is clearly the most efficient among all the schemes.

3.3. **Example 3: 1D Euler equations of gas dynamics, Sod shock tube problem.** We continue with 1D Euler equations of gas dynamics on $\Omega = (0, 1)$ with the initial condition

$$(\rho, v, p)(x, 0) = \begin{cases} (1, 0, 1) & \text{if } x \leq 0.5, \\ (0.125, 0, 0.1) & \text{if } x > 0.5, \end{cases}$$

and left and right Dirichlet boundary conditions corresponding to the shock tube problem proposed by Sod [13]. We run the simulation until $T = 0.1$ with a resolution of $N = 200$ points and compare the third- and fifth-order HENO schemes (with $\lambda = 0.9925$ and $\lambda = 0.995$, respectively) with

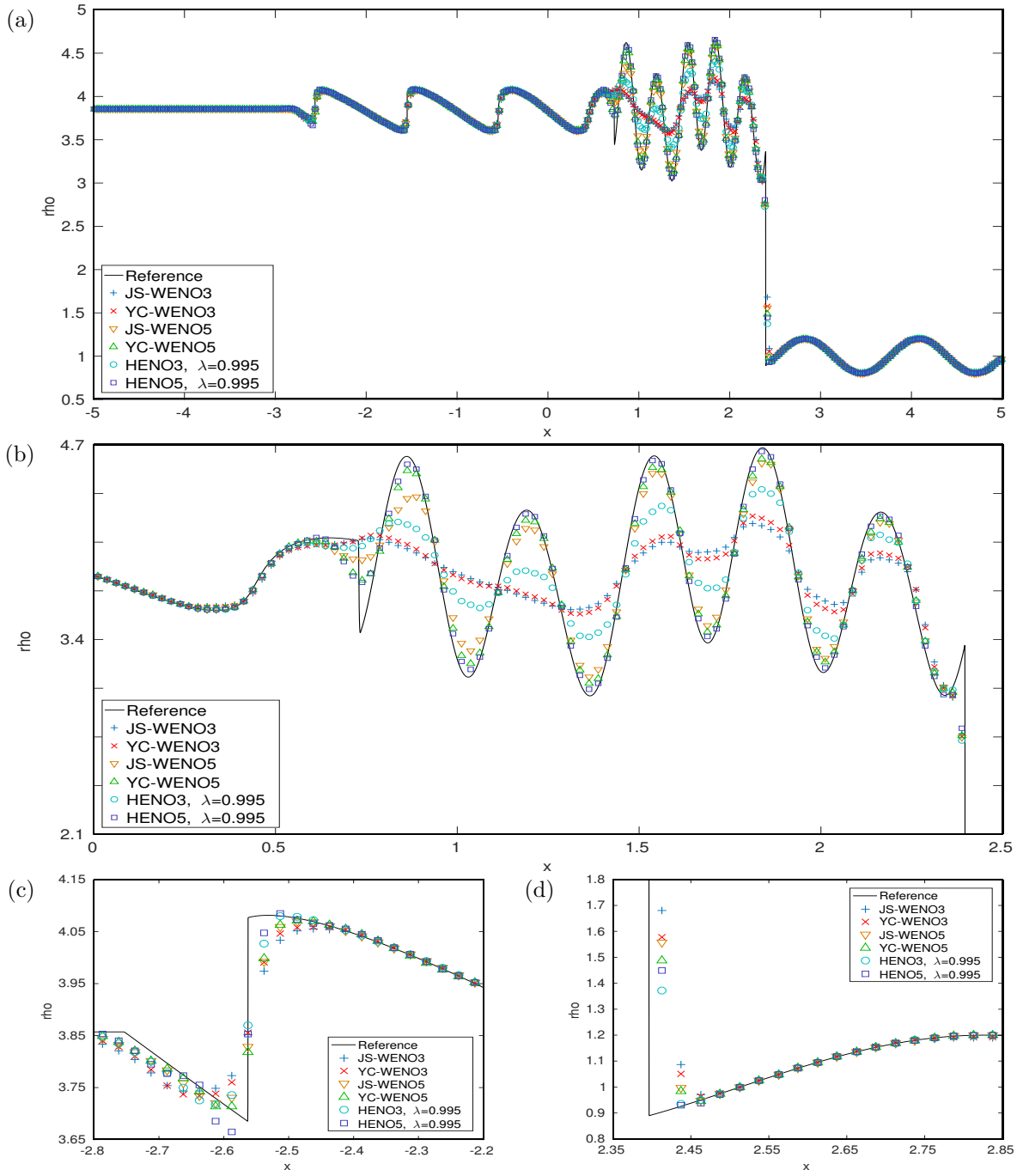

FIGURE 4. Example 2b (Shu-Osher problem, 1D Euler equations of gas dynamics): (a) numerical solution with $N = 400$ at $T = 1.8$ produced by several WENO and HENO schemes, (b), (c), (d): enlarged views.

their corresponding JS-WENO and YC-WENO counterparts. The numerical results are depicted in Figures 5 (a) to (d). An efficiency comparison is presented in Figure 5 (d). It appears that

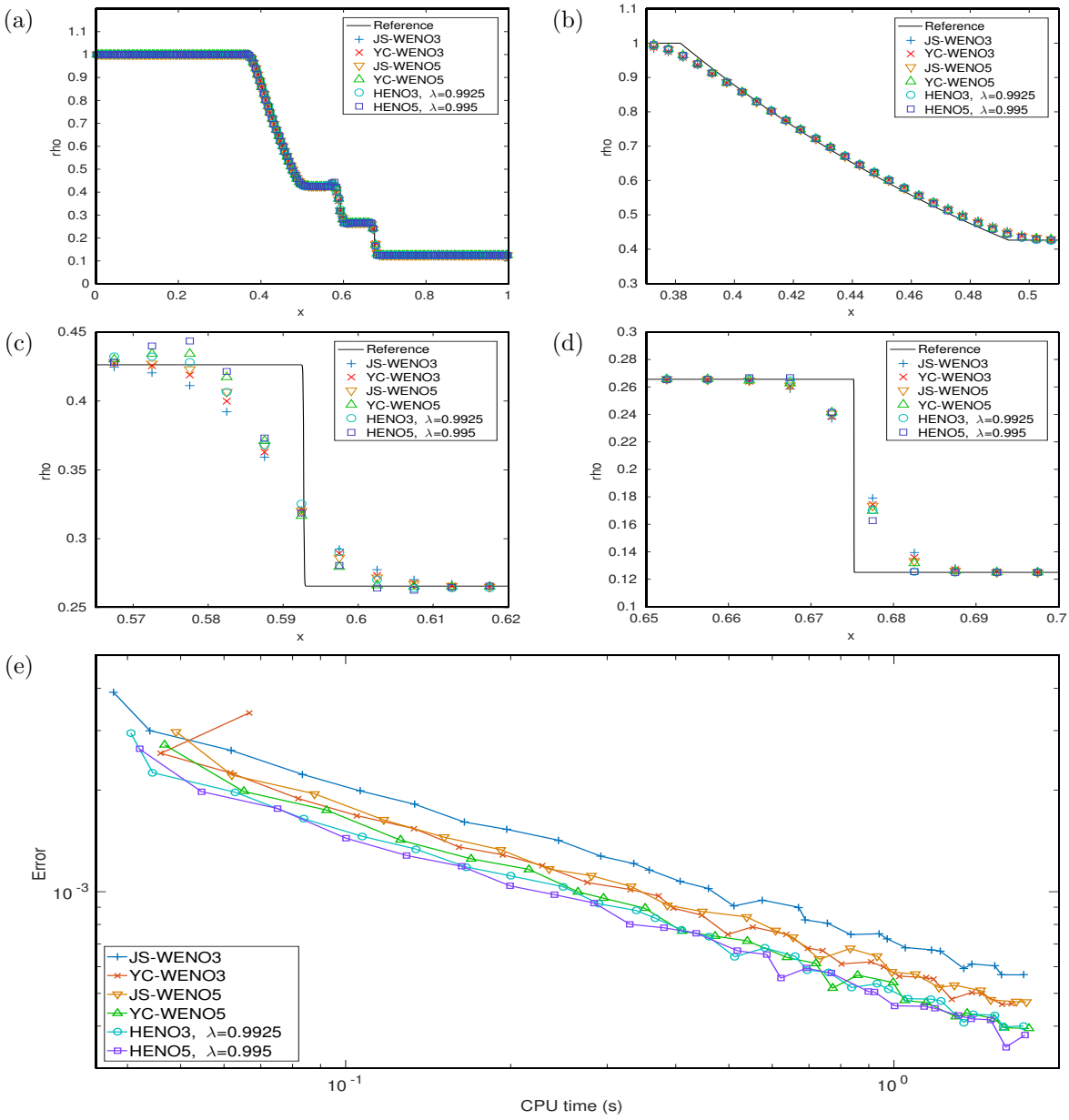

FIGURE 5. Example 3 (Sod shock tube problem, 1D Euler equations of gas dynamics): (a) numerical solution with $N = 200$ at $T = 0.1$ produced by several WENO and HENO schemes, (b), (c), (d): enlarged views, (e) efficiency plot.

in this case the schemes with less numerical viscosity (YC-WENO5 and HENO5, the latter with $\lambda = 0.995$) suffer from overshooting at the left of the contact, which aggravates as such numerical viscosity decreases. Thus, HENO5 is the scheme that presente more overshooting. As for the efficiency, we can observe that HENO schemes of both third- and fifth-order accuracy are slightly more efficient than all the WENO schemes used in this simulation.

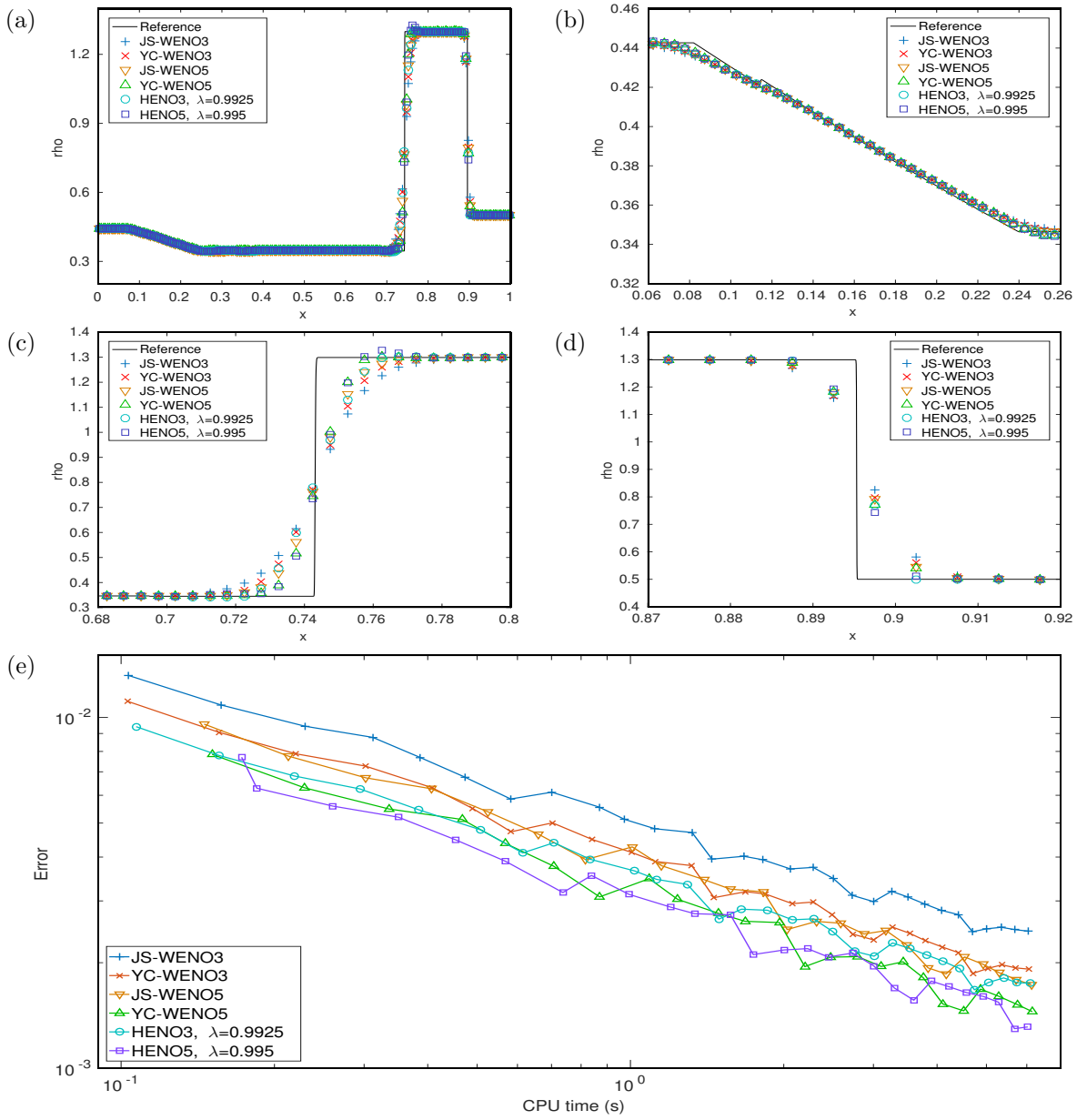

FIGURE 6. Example 4 (Lax shock tube problem, 1D Euler equations of gas dynamics): (a) numerical solution with $N = 200$ at $T = 0.16$ produced by several WENO and HENO schemes, (b), (c), (d): enlarged views, (e) efficiency plot.

3.4. **Example 4: 1D Euler equations of gas dynamics, Lax shock tube problem.** Again for the 1D Euler equations of gas dynamics on $\Omega = (0, 1)$, we now consider the initial condition

$$(\rho, v, p)(x, 0) = \begin{cases} (0.445, 0.69887, 3.5277) & \text{if } x \le 0.5, \\ (0.5, 0, 0.571) & \text{if } x > 0.5, \end{cases}$$

Order/Scheme	JS-WENO	YC-WENO	HENO
3	5.11	5.17	5.08
5	6.59	6.80	5.76
7	8.86	8.63	6.40
9	10.68	10.74	7.04

TABLE 2. Example 5 (Double Mach reflection, 2D Euler equations of gas dynamics): average CPU cost per iteration (seconds).

and left and right Dirichlet boundary conditions. We run a simulation until $T = 0.16$ and with a resolution of $N = 200$ points and perform the same comparisons than the previous example, using the same parameters λ for the HENO schemes. The numerical results are shown in Figures 6 (a) to (d) and the efficiency comparison is depicted in Figure 6 (e). We gain observe an overshoot to the right of the contact discontinuity, howeever this is less pronounced than in Example 3. It is again the scheme with smaller numerical viscosity, HENO5, for which the overshoot starts to become appreciable. This overshoot is reduced if the parameter λ is reduced accordingly. As for the efficiency plot, the results are similar as the previous example, except the fact that now YC-WENO5 is slightly more efficient than HENO3 with the chosen parameters.

3.5. **Example 5: 2D Euler equations of gas dynamics, Double Mach reflection.** The two-dimensional Euler equations for inviscid gas dynamics are given by

$$\boldsymbol{u}_t + \boldsymbol{f}^1(\boldsymbol{u})_x + \boldsymbol{f}^2(\boldsymbol{u})_y = 0,$$

with

$$\boldsymbol{u} = \begin{pmatrix} \rho \\ \rho v^x \\ \rho v^y \\ E \end{pmatrix}, \quad \boldsymbol{f}^1(\boldsymbol{u}) = \begin{pmatrix} \rho v^x \\ p + \rho (v^x)^2 \\ \rho v^x v^y \\ v^x (E + p) \end{pmatrix}, \quad \boldsymbol{f}^2(\boldsymbol{u}) = \begin{pmatrix} \rho v^y \\ \rho v^x v^y \\ p + \rho (v^y)^2 \\ v^y (E + p) \end{pmatrix}.$$

Here ρ is the density, (v^x, v^y) is the velocity, E is the specific energy, and p is the pressure that is given by the equation of state

$$p = (\gamma - 1) \left(E - \frac{1}{2} \rho ((v^x)^2 + (v^y)^2) \right),$$

where the adiabatic constant is again chosen as $\gamma = 1.4$. This experiment uses these equations to model a vertical right-going Mach 10 shock colliding with an equilateral triangle. By symmetry, this is equivalent to a collision with a ramp with a slope of 30° with respect to the horizontal line. For sake of simplicity, we consider the equivalent problem in a rectangle, consisting in a rotated shock, whose vertical angle is 30°. The domain is the rectangle $\Omega = [0, 4] \times [0, 1]$, whose initial conditions are

$$(\rho, v^x, v^y, E)(x, y, 0) = \begin{cases} \boldsymbol{c}_1 = (\rho_1, v_1^x, v_1^y, E_1) & \text{if } y \leq 1/4 + \tan(\pi/6)x, \\ \boldsymbol{c}_2 = (\rho_2, v_2^x, v_2^y, E_2) & \text{if } y > 1/4 + \tan(\pi/6)x, \end{cases}$$

$$\boldsymbol{c}_1 = \big(8, 8.25\cos(\pi/6), -8.25\sin(\pi/6), 563.5\big), \quad \boldsymbol{c}_2 = (1.4, 0, 0, 2.5).$$

We impose inflow boundary conditions, with value $\boldsymbol{c}_1$, at the left side, $\{0\} \times [0, 1]$, outflow boundary conditions both at $[0, 1/4] \times \{0\}$ and $\{4\} \times [0, 1]$, reflecting boundary conditions at $(1/4, 4] \times \{0\}$

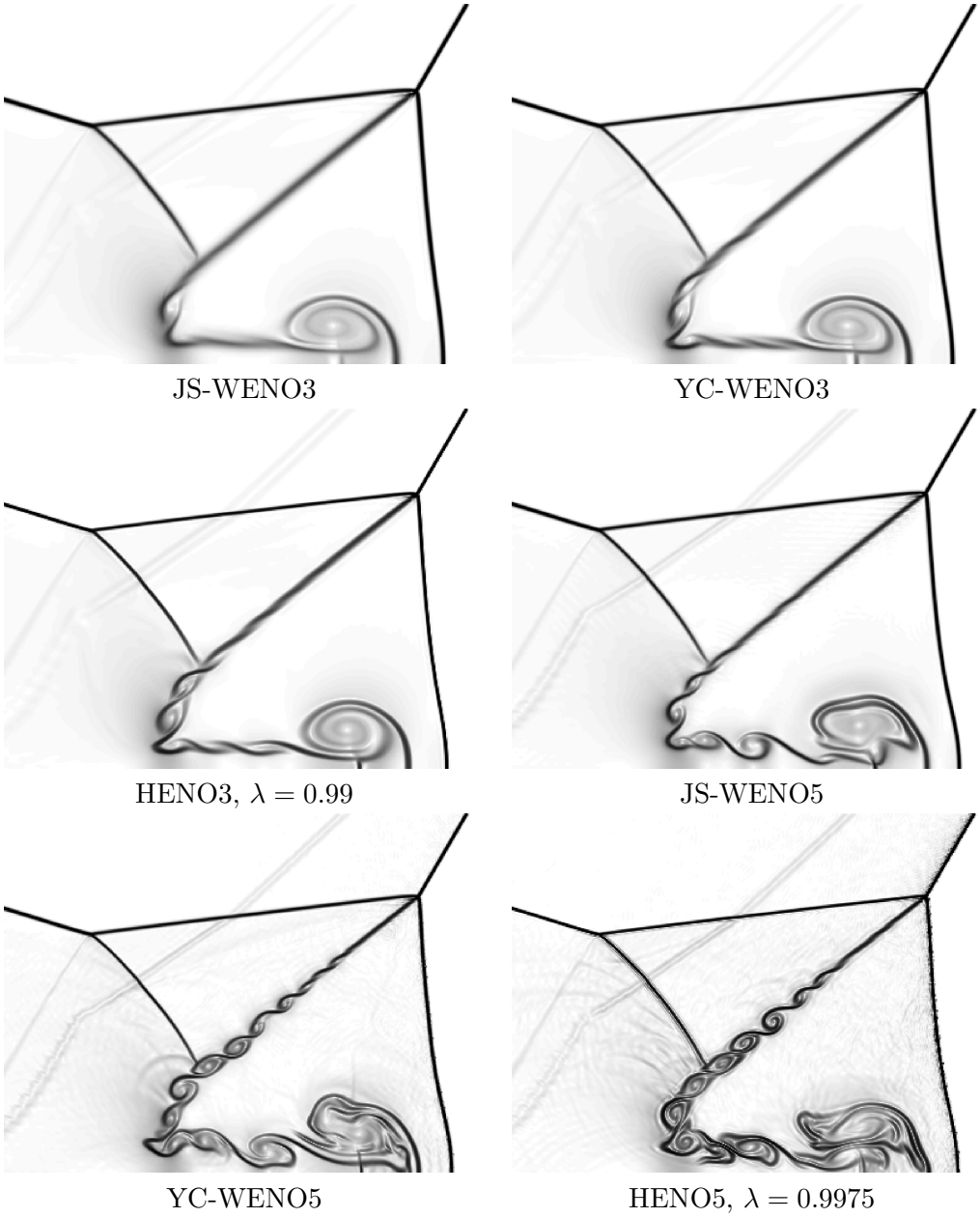

FIGURE 7. Example 5 (Double Mach reflection, 2D Euler equations of gas dynamics).

and inflow boundary conditions at the upper side, $[0,4] \times \{1\}$, which mimics the shock at its actual traveling speed:

$$(\rho, v^x, v^y, E)(x,1,t) = \begin{cases} \boldsymbol{c}_1 & \text{if } x \le 1/4 + (1+20t)/\sqrt{3}, \\ \boldsymbol{c}_2 & \text{if } x > 1/4 + (1+20t)/\sqrt{3}. \end{cases}$$

(Further details about this problem can be found in [14].) We run simulations until $T = 0.2$ at a resolution of 2048×2048 grid points with the same schemes as the 1D examples, using in this

Order/Scheme	JS-WENO	YC-WENO	HENO
3	24.35	23.69	24.12
5	30.25	30.39	26.89
7	40.12	38.72	30.08
9	46.88	47.49	32.38

TABLE 3. Example 6 (Riemann problem, 2D Euler equations of gas dynamics): average CPU cost per iteration (seconds).

case a parameter of $\lambda = 0.99$ for HENO3 and $\lambda = 0.9975$ for HENO5. The results are shown in Figure 7 and the computational cost associated to one time iteration is shown in Table 2 for all the combinations of schemes from orders 3 to 9. The results show that HENO3 scheme with $\lambda = 0.99$ has a similar resolution than a JS-WENO5 scheme, moreover with a lower computational cost. It is not possible to run simulations with significantly higher λ values (for instance, $\lambda = 0.9925$), since in this case this choice leads to negative physical quantities, yielding a blow-up of the simulation. As for the HENO5 scheme with $\lambda = 0.9975$, it can be observed that its resolution is slightly higher than YC-WENO5 and with less computational cost. We also see in the last two rows of the Table 2 that the benefits in terms of the lower computational costs of HENO schemes comparated to WENO schemes is even more remarkable for higher-order schemes. This is consistent with the fact that HENO schemes on uniform meshes have a linear increase of the computational cost as the order increases, whereas WENO schemes have a cubic increase of computational cost as the order increases.

3.6. **Example 6: 2D Euler equations of gas dynamics, Riemann.** Finally, we solve numerically a Riemann problem for the 2D Euler equations on the domain $(0,1)^2$. Riemann problems for 2D Euler equations were first studied in [10]. The initial data is taken from [7, Sect. 3, Config. 3]:

$$\boldsymbol{u}(x,y,0) = \big(\rho(x,y,0), \rho(x,y,0)v^x(x,y,0), \rho(x,y,0)v^y(x,y,0), E(x,y,0)\big)^{\mathrm{T}}$$

and

$$\begin{pmatrix} \rho(x,y,0) \\ v^x(x,y,0) \\ v^y(x,y,0) \\ p(x,y,0) \end{pmatrix}^{\mathrm{T}} = \begin{cases} (1.5,0,0,1.5) & \text{for } x > 0.5,\ y > 0.5, \\ (0.5323,1.206,0,0.3) & \text{for } x \le 0.5,\ y > 0.5, \\ (0.138,1.206,1.206,0.029) & \text{for } x \le 0.5,\ y \le 0.5, \\ (0.5323,0,1.206,0.3) & \text{for } x > 0.5,\ y \le 0.5, \end{cases}$$

with the same equation of state as in the previous test. The simulation is run until $T = 0.3$ at a resolution of 2048×2048 grid points using the same combination of schemes as in the previous example, where $\lambda = 0.9975$ is used for HENO3 scheme and $\lambda = 0.9995$ for HENO5 scheme, since in this case the problem allows schemes with much less numerical viscosity than the previous one. The results are depicted in Figure 8 and a comparison of the numerical cost of each time iteration is shown in Table 3

From the numerical results we can conclude that again HENO3 with the chosen parameter has a similar resolution than JS-WENO5 while having a lower computational cost. As for HENO5 scheme with the selected parameter, which is very close to 1, its low numerical viscosity yields a result with a much higher resolution than even YC-WENO5, using in turn a lower amount of computational time. We also observe again that for higher order schemes the increase of the computational cost in HENO schemes is much slower than in the case of WENO schemes.

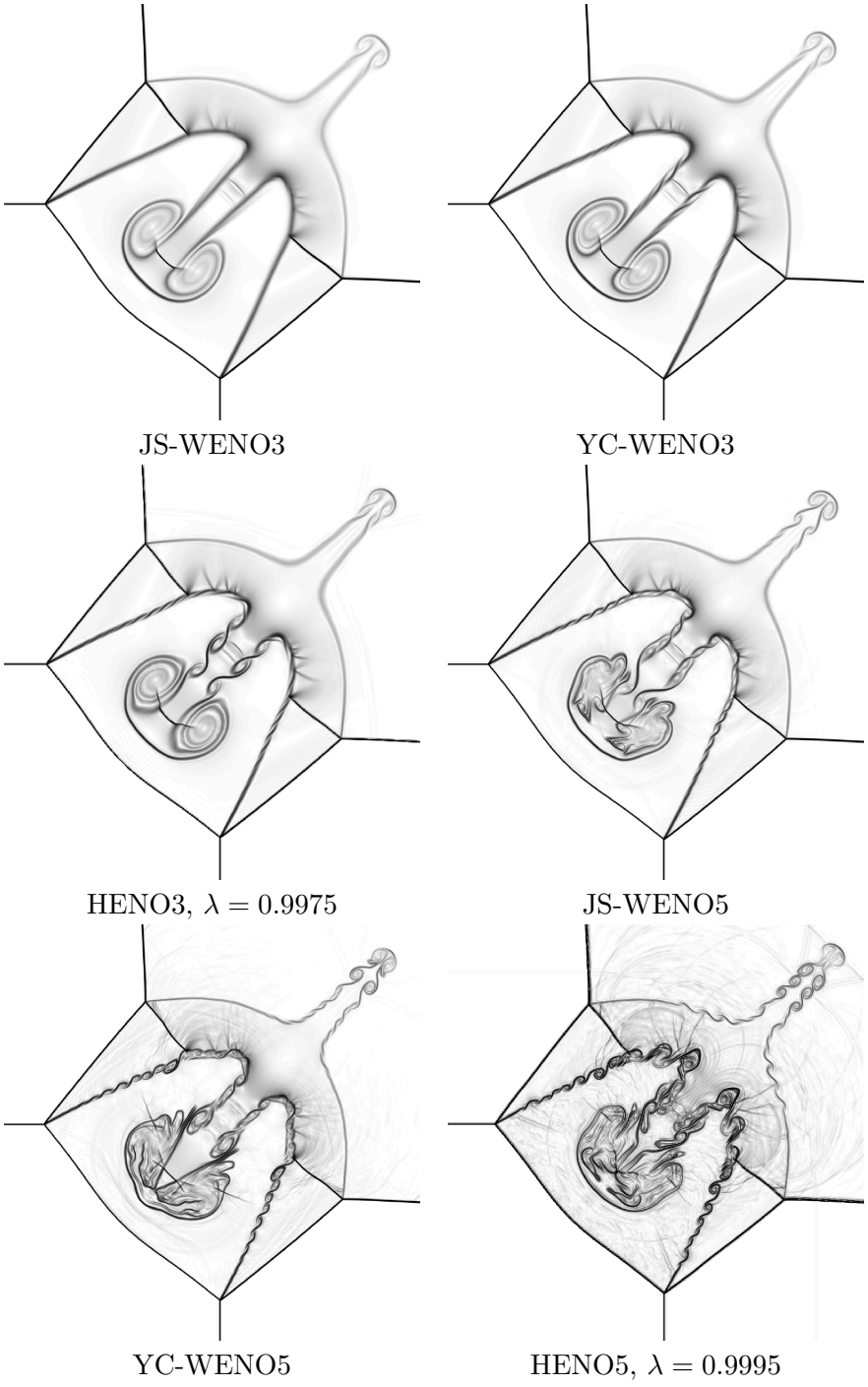

FIGURE 8. Example 6 (Riemann problem, 2D Euler equations of gas dynamics).

4. Conclusions

In this paper we have presented a novel high-order reconstruction method that can be used as an alternative interpolator competitive with WENO methods. The main benefits of our proposal are

the following ones. First, we have efficiency on uniform meshes, with linear cost with respect to the order, in contrast with the cubic cost with respect to the order of the traditional WENO schemes. In second place, ease of implementation on non-uniform meshes, with quadratic cost with respect to the order, the same as the classical interpolation algorithm without detection of discontinuities on non-uniform meshes. In third place, the reconstruction point x^* can be placed anywhere without affecting the discontinuity detection; therefore, this reconstruction algorithm can be applied in other contexts, such as high-order extrapolation for numerical boundary conditions to generate values into ghost cells. In fourth place, the amount of numerical viscosity can be controlled continuously through the parameter λ. In fifth place, if λ is properly tuned, the results are better than the WENO schemes of the corresponding order, yielding a scheme with genuine $(2r-1)$-th order. Finally, the reconstruction algorithm is a hybridization of a first-order and a $(2r-1)$-th order interpolation. This yields ultimately also a global hybrid numerical scheme, which is first-order accurate for $\lambda = 0$, $(2r-1)$-th order shock-capturing scheme for $0 < \lambda < 1$ and a pure $(2r-1)$-th order scheme for $\lambda = 1$. Of course, one of the main shortcomings of this proposal consists in the need to properly tune the hybridization parameter in order to obtain results competitive and/or better than those obtained with the best WENO schemes. However, we have seen in the numerical experiments that for both third and fifth order schemes it suffices with setting the parameter around the value 0.99 in order to obtain good results while keeping the non-oscillatory behaviour.

The numerical results obtained also show that in general the order recovery near sharp discontinuities is not actually relevant, since we have obtained results of a similar or even better quality than WENO schemes, with order recovery of order r near discontinuities, by just combining a high $(2r-1)$ order reconstruction with a low (first) order reconstruction acting when a discontinuity crosses the stencil. In fact, the results show that it suffices to make the weight ω_λ take values as favorable as possible to the high order reconstructions, while allowing it to drop the order near sharp discontinuities, yielding a scheme with low numerical viscosity.

In a future work, we encompass performing a deeper analysis involving optimal λ choices as well as suitable redesigns of ω_λ in order to attain formally the optimal accuracy regardless of the order of a critical point.

Acknowledgements

RB is supported by CONICYT/PIA/Concurso Apoyo a Centros Científicos y Tecnológicos de Excelencia con Financiamiento Basal AFB170001; Fondecyt project 1170473; and CRHIAM, project CONICYT/FONDAP/15130015. DZ is supported by Conicyt (Chile) through Fondecyt project 3170077 and Spanish MINECO project MTM2017-83942-P.

References

[1] F. Aràndiga, A. Baeza, A.M. Belda, P. Mulet, Analysis of WENO schemes for full and global accuracy, SIAM J. Numer. Anal. 49 (2011) 893–915.

[2] A. Baeza, R. Bürger, P. Mulet, D. Zorío: On the efficient computation of smoothness indicators for a class of WENO reconstructions. Preprint 2018-37, Centro de Investigación en Ingeniería Matemática, Universidad de Concepción, 2018.

[3] R. Borges, M. Carmona, B. Costa, W.S. Don, An improved weighted essentially non-oscillatory scheme for hyperbolic conservation laws, J. Comput. Phys. 227 (2008) 3191–3211.

[4] R. Donat, A. Marquina, Capturing shock reflections: An improved flux formula, J. Comput. Phys. 125 (1996) 42–58.

[5] R. Eymard, T. Gallouët, R. Herbin, Handbook for Numerical Analysis VII, Ph. Ciarlet, J.L. Lions eds, North Holland (2000) 715-1022.

[6] A.K. Henrick, T.D. Aslam, J.M. Powers, Mapped weighted essentially non-oscillatory schemes: Achieving optimal order near critical points, J. Comput. Phys. 207 (2005) 542–567.

[7] A. Kurganov, E. Tadmor, Solution of two-dimensional Riemann problems for gas dynamics without Riemann problem solvers, Numer. Methods Partial Differential Equations 18 (2002) 584–608.
[8] G.S. Jiang, C.-W. Shu, Efficient implementation of Weighted ENO schemes, J. Comput. Phys. 126 (1996) 202–228.
[9] X.-D. Liu, S. Osher, T. Chan, Weighted essentially non-oscillatory schemes, J. Comput. Phys. 115 (1994) 200–212.
[10] C.W. Schulz-Rinne, Classification of the Riemann problem for two-dimensional gas dynamics, SIAM J. Math. Anal. 24 (1993) 76–88.
[11] C.-W. Shu, S. Osher, Efficient implementation of essentially non-oscillatory shock-capturing schemes, J. Comput. Phys. 77 (1988) 439–471.
[12] C.-W. Shu, S. Osher, Efficient implementation of essentially non-oscillatory shock-capturing schemes, II. J. Comput. Phys. 83 (1989) 32–78.
[13] G.A. Sod, A survey of several finite difference methods for systems of nonlinear hyperbolic conservation laws, J. Comput. Phys. 27 (1978) 1–31.
[14] P. Woodward, P. Colella, The numerical simulation of two-dimensional fluid flow with strong shocks, J. Comput. Phys. 54 (1984) 115–173.
[15] N.K. Yamaleev, M.H. Carpenter, Third-order energy stable WENO scheme, J. Comput. Phys. 228 (2009) 3025–3047.
[16] N.K. Yamaleev, M.H. Carpenter, A systematic methodology to for constructing high-order energy stable WENO schemes, J. Comput. Phys. 228 (2009) 4248–4272.
[17] D. Zorío, A. Baeza, P. Mulet, An approximate Lax-Wendroff-type procedure for high-order accurate schemes for hyperbolic conservation laws, J. Sci. Comput. 71 (2017) 246–273.